ACS OMEGA

Open Access

http://pubs.acs.org/journal/acsodf

Article

Biogenic Synthesis of Copper Oxide Nanoparticles from *Aloe vera*: Antibacterial Activity, Molecular Docking, and Photocatalytic Dye Degradation

Sabeeha Jabeen, Vasi Uddin Siddiqui,* Shashi Bala, Nidhi Mishra, Anamika Mishra, Rubina Lawrence, Pratibha Bansal, Abdul Rahman Khan, and Tahmeena Khan*

Cite This: *ACS Omega* 2024, 9, 30190−30204

Read Online

ACCESS | Metrics & More | Article Recommendations

ABSTRACT: Green synthesis methods offer a cost-effective and environmentally friendly approach to producing nanoparticles (NPs), particularly metal-based oxides. This study explores the green synthesis of copper oxide nanoparticles using *Aloe vera* (*Aloe barbadensis* Miller) leaf extract. The characterization revealed a unique sago-shaped morphology revealed by field-emission scanning electron microscopy and X-ray diffraction analysis. Distinctive metal−oxygen bonds at 521 and 601 cm^{-1} were confirmed by Fourier-transform infrared (FT-IR) spectroscopy. Furthermore, UV−visible spectroscopy revealed absorbance at 248 nm, suggesting electron transitions across energy bands and varying surface conduction electrons. The band gap value indicated the presence of quantum confinement effects, which were probably caused by the distinctive morphology and surface structure of the biogenic NPs. Additionally, molecular docking studies were carried out against key proteins of *Salmonella typhi* and *Listeria monocytogenes,* namely, listeriolysin O (PDB ID: 4CDB), internalin (InlA) (PDB ID: 1O6T), *Salmonella* effector protein (SopB) (PDB ID: 4DID), and YfdX (PDB ID: 6A07) using AutoDock 4.2. The results revealed binding energies against *S. typhi* and *L. monocytogenes* proteins, indicating potential interactions establishing the foundation for further in-depth understanding of the molecular basis underlying the observed antibacterial effects *in vitro* against *S. typhi*, *Klebsiella pneumoniae*, *Pseudomonas aeruginosa*, and *L. monocytogenes*. Antibacterial activity evaluation yielded impressive results, with CuO NPs displaying significant activity against *S. typhi* and *L. monocytogenes*, exhibiting zones of inhibition values of 13 ± 0.02 and 15 ± 0.04 mm, respectively. Moreover, the CuO NPs demonstrated remarkable photocatalytic efficacy, resulting in the degradation of 77% of the methylene blue dye when exposed to UV irradiation. This study highlighted the potential of green-synthesized CuO NPs derived from *A. vera* with their unique morphology, interesting spectroscopic properties, and promising antibacterial and photocatalytic activities.

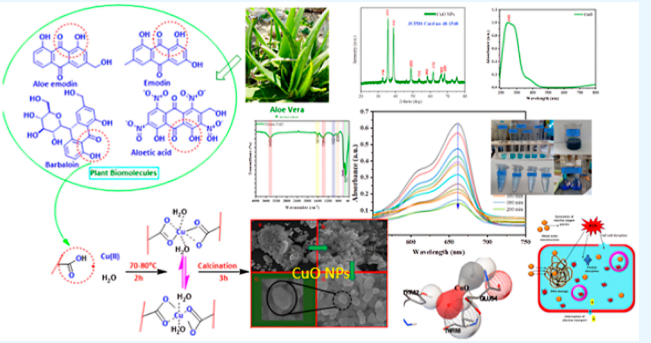

1. INTRODUCTION

Nanotechnology is a vast field encompassing the physical, chemical, and environmental sciences. Scientific exertions toward the fabrication and exploration of metal oxide-based nanoparticles (NPs) have expanded due to their diverse applications in biomedicine, farming, food, cosmetics, paints, photocatalysis, and textiles.[1] The NPs based on metal oxides exhibit distinctive sizes and outstanding physicochemical properties.[2−4] Many techniques are used to fabricate metal oxide-based NPs, some of them being hydrothermal,[5] coprecipitation,[6] sonication,[7] and sol−gel,[8] which are costly and extensive, involve hazardous chemicals, and release toxic byproducts. In addition, the NPs fabricated by the chemical process are loaded with toxic substances on their surface and are considered unsuitable for biological and therapeutic applications. Therefore, alternate strategies for the fabrication of NPs have emerged, including green synthesis, which is assisted by the various phytoconstituents such as flavonoids that act as reducing and capping agents.[9] Biological strategies involving plant extracts or organisms like bacteria, algae, and fungi are being considered as environment-friendly.[10] Plant extract-based synthesis of NPs is more suitable than the other biological approaches as it does not require cell cultures.[11] Furthermore, the synthesis involves safe handling and easy

Received: December 19, 2023
Revised: February 12, 2024
Accepted: May 9, 2024
Published: July 1, 2024

availability associated with plants and the abundance of metabolite content, which aids the process of reduction.[12] Iron oxide (Fe_2O_3) NPs prepared by the seed extract of *Psoralea corylifolia*[13] possessed excellent anticancer activity, and the flower extract of *Avicennia marina*[14] has been tested for dye degradation. *Kappaphycus alvarezii*[15] plant extract has been tested for photocatalytic and antibacterial activities. Furthermore, TiO_2 NPs synthesized by *Kniphofia foliosa* root extract have been tested for their antibacterial activity and the leaf extract of *Trigonella foenum-graecum*.[16] CuO NPs have found miscellaneous applications including gas detection,[17] catalysis,[18] and solar energy conversion.[19] They have also been shown to possess antioxidant properties and have also been explored for their antimicrobial properties.[20] Chemical composition, crystal morphology, and surface area to volume ratio are some of the factors that influence their overall activity. CuO NPs have been fabricated using *Annona muricata* L extract and tested for their anticancer activity against AMJ-13 and MCF-7 breast cancer cell lines and breast epithelial cell line (HBL-100). The findings suggested reduced cell proliferation of the breast cancer cell lines. Furthermore, enhanced production of lactate dehydrogenase was observed, which might have been caused by cell membrane damage.[21] In another study, CuO NPs fabricated from *Averrhoa carambola* leaf extract were tested for their antibacterial activity against *Bacillus megaterium*, *Staphylococcus aureus*, *Escherichia coli*, *Salmonella typhi*, and *Pseudomonas aeruginosa*. High zones of inhibitions (26 and 24 nm) were obtained against *S. typhi* and *E. coli*, respectively.[22] An environment-friendly and simple method for the synthesis of nearly monodisperse CuO nanospheres (NSPs) using the leaf extracts of *Phyllanthus reticulatus* and *Conyza bonariensis* as novel green reducing agents has been reported.[23] The method was not only novel and cost-effective, but also found to be convenient for large-scale commercial production and health-related applications of CuO NPs.[24] Although the antimicrobial activity of CuO NPs is known, a deeper understanding of the mechanistic insight is still needed, which can be done computationally through molecular docking studies needing further exploration. It is very important to comprehend the protein−metal binding and the complex formed during the interaction between nanomaterials and the biomolecules, and that has led to the utility of molecular docking which predicts the cooperation affinity of the protein−metal complex and also the hindrances and limitations where the binding is not feasible. Molecular docking studies have also been undertaken with Fe_2O_3 and Fe_3O_4 NPs with the spike protein binding domain (S1-RBD) of SARS-CoV-2. Hydrophobic interactions of Fe_3O_4 were also formed with Leu455, Ser494, and Phe497. The energy minimization was done through the Ligand Preparation Protocol of Accelry's Discovery Studio 4.1.[25] In another study, molecular docking of NiO NPs with genetic molecules was studied to explore their toxicity.[26] Other than the medicinal properties, metal oxide-based NPs have also been explored for their photocatalytic activity. CuO NPs exhibit a large surface area, good redox potential, excellent electrochemical activity, superthermal conductivity, and good stability required for a good photocatalyst.[27] CuO NPs prepared by the leaf extract of *A. muricata*[28] possessed outstanding photocatalytic activity, whereas those fabricated from the leaf extract of *Psidium guajava*[29] have also been tested for dye degradation. Similarly, CuO NPs synthesized from the leaf extract of *Amaranthus dubius*[30] have been tested for photocatalytic and sensor activities. In a very recent study, the fruit extract of *Abelmoschus esculentus* was used to fabricate CuO NPs, which were later on tested for their cytotoxic and photocatalytic activity.[31]

The present investigation reports the green fabrication of CuO NPs from *Aloe barbadensis* plant belonging to the Xanthorrheaceae family. Traditionally, the *Aloe vera* plant has been used widely for medicinal purposes and shows a variety of medicinal activities such as antioxidant, antibacterial, dental plaque removal, blood sugar control, and treatment of canker sores.[32] Approximately 80 chemical constituents have been isolated from the exudate, by liquid chromatography, with anthraquinone *C*-glycosides, anthrones, chromones, phenyl pyrones, and naphthalene derivatives being the most abundant phenolic compounds and particularly polyphenols Aloe-emodin, anthranol, aloin A and B (barbaloin), isobarbaloin, and emodin, etc., which may act as stabilizing and reducing agents.[33,34] Molecular docking studies of CuO NPs have been reported with multiple antibiotic resistance regulators (mmrR), a part of the multidrug-resistance group protein through AutoDock Vina. A docking score of −2.1 kcal/mol was obtained and the NPs interacted with the Asn126, Val142, and Leu123 amino acid residues.[35] In another study, CuO NPs were docked against PhoQ, which acts as a membrane-associated protein kinase that undergoes autophosphorylation and a component of *Salmonella typhimurium*'s signaling system causing endocytosis. A binding score of −2.1 kcal/mol was obtained against the selected protein.[36] The molecular docking studies were performed with four antibacterial target proteins, namely, listeriolysin O, internalin (InlA), SopB, and YfdX. The photocatalytic activity was also performed on Methylene Blue (MB) dye, which has several applications such as in the paper, dyeing, textile, pharmaceutical, printing, paint, medicine, and food industries.[37] In the textile industry, the most commonly used dye is MB. Textile industries generally discharge a huge amount of MB dye solution in natural water sources, becoming a health threat to humans and aquatic life due to its toxic, carcinogenic, and nonbiodegradable nature, which causes serious diseases such as respiratory distress, abdominal disorders, blindness, and digestive and mental disorders.[38] Table 1 represents a comparison between the previous literature and the current study in terms of the novelty of the work, which also includes important parameters like the reaction time, pH, and temperature.

2. EXPERIMENTAL DETAILS

2.1. Materials and Methods. The cultivated *A. barbadensis* Miller was obtained from the garden of the University of Lucknow, Hasan Ganj, Lucknow, India (26.8633° N, 80.9360° E). Copper nitrate trihydrate [$Cu(NO_3)_2{\cdot}3H_2O$], sodium hydroxide (NaOH), MB, and distilled water were purchased from Thermo Fisher Scientific, Delhi, India. For structural morphology determination, field-emission scanning electron microscopy studies were performed on a Zeiss Gemini SEM microscope operating at an accelerating voltage of 3 kV. EDX analysis was supported by a Bruker energy-dispersive X-ray spectrometer (EDX). The FT-IR spectrum was recorded on a Bruker Tensor 37 spectrometer between the range of 400−4000 cm^{-1} through the KBr pellet method. The X-ray diffraction (XRD) spectrum was recorded on a Rigaku Ultima IV instrument for phase purity and crystallinity, and the UV−visible spectrum was recorded on a Hitachi U3900 spectrometer. The bacterial strains used in the

https://doi.org/10.1021/acsomega.3c10179
ACS Omega 2024, 9, 30190−30204

Table 1. Comparison between the Present Study and Previous Studies for the Synthesis of *A. vera*-Mediated CuO NPs

precursor	method	plant source	reaction time	reaction pH	reaction temperature (°C)	application studied	computational studies	morphology and size	refs
$CuSO_4{\cdot}5H_2O$	green synthesis	*A. vera* extract	7 h		130	optical properties	not reported	spherical, 20 nm	39
$Cu(NO_3)_2{\cdot}3H_2O$	green synthesis	*A. vera* extract	24 h		100−120	bacterial fish pathogens *Aeromonas hydrophila*, *Pseudomonas fluorescens*, and *Flavobacterium branchiophilum*	not reported	spherical, 20 nm	40
$CuSO_4{\cdot}5H_2O$	green synthesis	*A. vera* extract	25 min		130	optical properties	not reported	-	41
$Cu(NO_3)_2{\cdot}3H_2O$	green synthesis	*A. vera* extract	72 h		110	antibacterial activity	not reported	spherical, 30 nm	42
$(Cu(CH_3COO)_2{\cdot}H_2O)$	biogenic synthesis	*A. vera* extract	4 h	11.5	70	antibacterial activity	not reported	capsule and spherical fluffy-like arrangement, 5−20 nm	43
$Cu(NO_3)_2{\cdot}3H_2O$	solvothermal preparation	polyethylene glycol (PEG) 8000 with hydrazine hydrate	8 h		200	cytotoxic activity and antibacterial activity	not reported	spherical, 15 nm	44
$Cu(NO_3)_2{\cdot}3H_2O$	green synthesis	*A. vera* extract	4 h	10	70−80	antibacterial activity on *Klebsiella pneumoniae*, *S. typhi*, *P. aeruginosa*, and *L. monocytogenes*	reported in *S. typhi*, and *L. monocytogenes* bacterial protein	sago-shaped, 15.8 nm	**present work**

study were obtained from the Department of Industrial Microbiology, Sam Higginbottom University of Agriculture, Technology and Science, Prayagraj, India. Molecular docking was done using AutoDock 4.2, which is a freely available tool for docking analysis, on an Acer desktop with 8 GB of RAM and an Intel Core i5-4590 processor running at 3.30 GHz. The 3D structures of the target proteins, namely, listeriolysin O (PDB ID: 4CDB), internalin (InlA) (PDB ID: 1O6T), SopB (PDB ID: 4DID), and YfdX (PDB ID: 6A07) for docking were obtained from the Protein Data Bank (www.rcsb.org). The crystal structures of PgdA and *O*-acetyltransferase A (OatA) were not available on the PDB database, and their corresponding structures were modeled on the SWISS-MODEL web server.

2.2. Preparation of the *A. vera* Plant Extract. *A. vera* plant leaves (40 g) were washed with tap water, followed by distilled water to remove the dirt and other impurities, and dried well. The leaves were sliced into very tiny parts, ground, and then boiled for 60 min at 50−70 °C with 200 mL of distilled water in a 500 mL round bottle flask using Soxhlet apparatus, a standard method to extract the phytochemicals from the plants. These phytochemicals consist of polyphenols and can be subdivided into flavonoids and nonflavonoid groups. These polyphenols act as a stabilizing and reducing agent for the synthesis of nanomaterials.[47] After the mixture was allowed to reach room temperature, the resultant mixture was filtered with the help of a strainer to eradicate any solid content and finally filtered via Whatman filter paper (grade 1). The filtrate was stored at 4 °C in a refrigerator for the synthesis of CuO NPs.

2.3. Synthesis of CuO NPs. 100 mL of 0.1 M $Cu(NO_3)_2{\cdot}3H_2O$ solution was prepared in distilled water in a 500 mL beaker, and 20 mL of *A. vera* plant extract was slowly mixed with continuous stirring at 70−80 °C on a magnetic stirrer. This was followed by the dropwise addition of freshly prepared 0.2 mmol NaOH into the reaction solution to maintain a pH of 10 (Figure 1a). After 4 h of vigorous stirring, the mixture was collected upon settling down. The collected precipitate of CuO NPs was washed 4−5 times with distilled water followed by ethanol, dried on a watch glass transferred to a crucible, and calcined in a muffle furnace at 420 °C for 3 h before further use. The material was heated in the muffle furnace to obtain uniform CuO NPs.[45] It has been reported earlier that the overall surface area of the NPs decreases with the increasing calcination temperature, and the photocatalytic degradation is affected by thermal treatment. Usually, the surface area at the calcination temperature of 400 and 500 °C is higher as compared to that at 300 and 500 °C.[46] The NPs were obtained in 91% yield. The proposed reaction mechanism is depicted in (Figure 1b).

2.4. Molecular Docking. Different computational approaches have been employed to study the interaction between the NPs and the biological targets. Density functional theory, molecular docking, kinetic mean-field model, and molecular dynamics simulations were explored to comprehend how the NPs behave within a biological system.[47] Molecular docking has emerged as an efficient tool to explore potential drug candidates. The tool can also be used to predict potential side effects or toxicities. In molecular docking, the 3D structures of ligand and target molecules are visualized first in their most preferred binding orientations, and then the binding energy released upon formation of a stable complex is assessed. In the

https://doi.org/10.1021/acsomega.3c10179
ACS Omega 2024, 9, 30190−30204

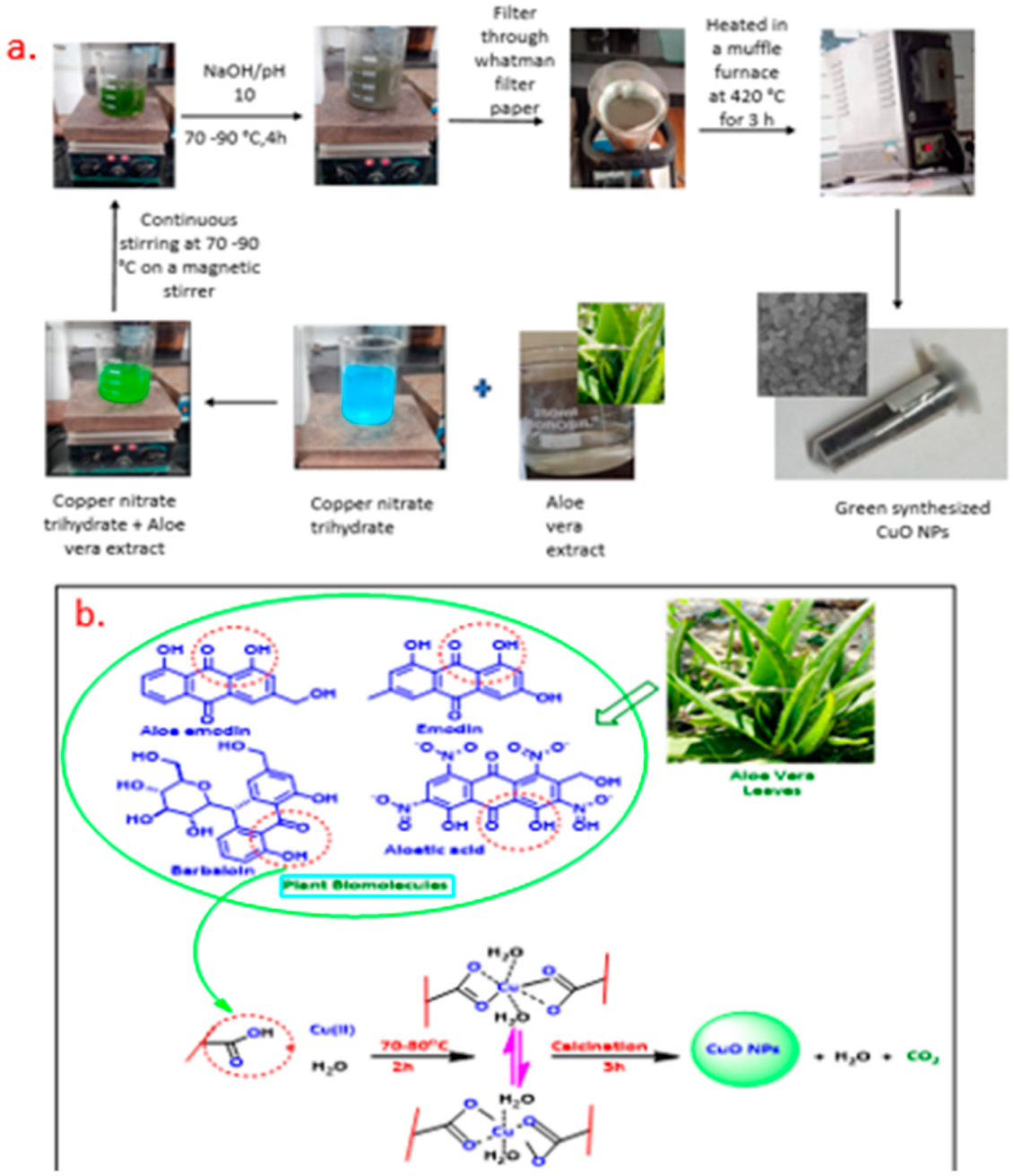

Figure 1. (a) Schematic representation of the synthesis of CuO NPs and (b) proposed reaction mechanism of the formation of CuO NPs.

present study, molecular docking was done on AutoDock 4.2, which is a freely available tool for docking analysis.

2.4.1. Formation of Protein. The 3D structures of the target proteins, namely, listeriolysin O (PDB ID: 4CDB), internalin (InlA) (PDB ID: 1O6T), SopB (PDB ID: 4DID), and YfdX (PDB ID: 6A07) for docking were taken from PDB. The crystal structures of PgdA and OatA were not available on the PDB database, so their corresponding structures were modeled. Modeling of proteins PgdA and OatA was carried out on the SWISS-MODEL web server. The Swiss model, a widely used and effective tool for predicting protein structure, is based on the homology principle.[48] The query protein's amino acid sequence is given as input, and after a thorough search for the template structure based on similarity scores, the structure of the query protein is predicted. The amino acid sequences of the respective proteins, namely, PgdA and OatA, were obtained from the National Centre for Biotechnology Information (NCBI) platform and utilized as input for modeling. The proteins were prepared before docking, and the Hetatm was removed from the protein structure; also, the proteins were checked for the missing atoms and repaired. The proteins were further prepared by adding hydrogen and charges, and the prepared proteins were then saved in the .pdbqt format. Lamarckian genetic algorithms were used for docking calculations. AutoDock 4.2 does not come with parameters for copper ions by default, and therefore, the appropriate parameters for copper were taken from literature[49] and used for the grid preparation and docking. The grid parameters were set as 126 × 126 × 126.

2.4.2. Ligand Preparation. The CuO NPs were sketched on Avogadro, and the file was saved in the .pdb format and

https://doi.org/10.1021/acsomega.3c10179
ACS Omega 2024, 9, 30190−30204

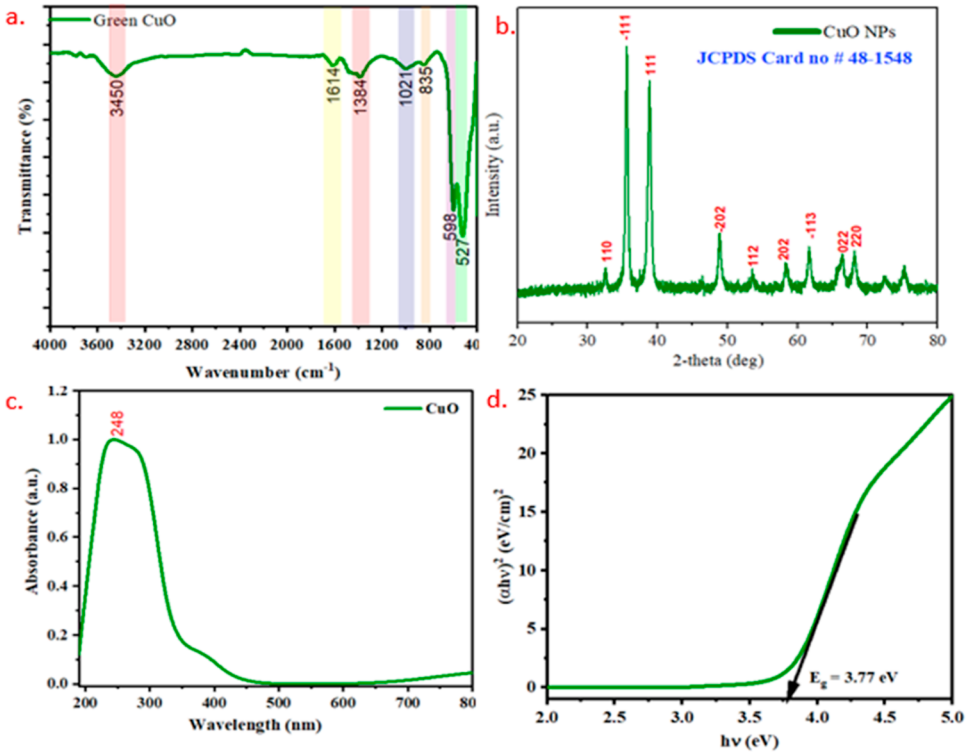

Figure 2. (a) FT-IR spectrum of the synthesized CuO NPs, (b) XRD spectrum of the synthesized CuO NPs, (c) UV−vis spectrum of the synthesized CuO NPs, and (d) Tauc's plot of the synthesized CuO NPs.

converted to the .pdbqt format by the online conversion tool Open Babel.

2.4.3. Homology Modeling. The crystal structure of PgdA and OatA in the PDB database was unavailable. So, their structures were obtained through homology modeling. The modeling was brought out on the SWISS-MODEL web server. The amino acid arrangements of the respective proteins were utilized for homology modeling. The amino acid arrangements of the proteins, namely, PgdA and OatA, were obtained from the NCBI with accession numbers WDE52696 (PgdA) and CAF1694382 (OatA) and were utilized as input for modeling on the SWISS-MODEL web server. The amino acid arrangement of the query proteins was utilized for the search of the template protein by the SWISS-MODEL server. Based on the similarity score with the suitable template structure, parameters such as global model quality estimation (GMQE) and qualitative model energy analysis (QMEAN) were considered for the modeling. The acceptable range for GMQE is between 0 and 1, while the QMEAN below 4 is considerable.[50] The SWISS-MODEL predicts the most suitable structure of the query protein considering the parameters of similarity, GMQE, and QMEAN. The Ramachandran plot was also obtained for the assessment of the modeled protein structures.

2.5. Antimicrobial Activity Assessment. Antibacterial activity assessment was done by the agar well diffusion method as follows.

2.5.1. Methodology. Nutrient agar (NA) (2.8 g in distilled water) and potato dextrose agar (3.9 g in distilled water) plates were swabbed with 8 h broth culture of each organism.[51] A sterile cork drill is used to drill three holes (10 mm diameter, approximately 2 cm apart) in each plate. Solutions of each compound (sample, antibiotic streptomycin, and blank) were set up in distilled water with a concentration of 1 mg/mL. An overnight broth culture of the tested bacteria was streaked onto a NA plate, and a 5 mm width well was made and occupied. 100 μL of working solution (1 mg/mL) was added and left for 1 h. The plates were then incubated at 37 ± 1 °C for 24−48 h. High-impact wells were measured with the help of a Himedia zone ruler. Experiments were executed in triplicate and interpreted accordingly.

2.6. Photocatalytic Activity Assessment. The photocatalytic activity of the synthesized CuO NPs was measured under UV light. The photocatalytic reaction was monitored in a Pyrex flask reactor. 40 mg of CuO NPs was added to 100 mL of MB dye aqueous solution (10 ppm), and the suspension was magnetically stirred for 20 min to create equipoise on the dye surface in the dark. The stabilized suspension was then illuminated with a 6A UV lamp (Philips, India). UV rays were passed perpendicularly on the surface of the reaction mixture with a maximum intensity of 365 nm. The distance between the reaction mixture and the UV lamp was 14 cm. After a certain time (20 min interval), an aliquot of the solution was analyzed with a UV−vis spectrophotometer to examine the absorption behavior of the eluted dye solution. While taking the portion out for analysis, the UV−visible lamp was stopped. In general, dye degradation reactions follow pseudo-first-order kinetics. The degradation efficiency according to the absorbance value can be obtained from eq 1.

$$\text{Degradation efficiency} = C_0 - C_t/C_0 \times 100 \quad (1)$$

So, C_0 = initial concentration of the dye and C_t is the dye concentration after time (t).

3. RESULTS AND DISCUSSION

3.1. FT-IR Analysis. The FT-IR analysis was carried out between 400 and 4000 cm^{-1} to identify the functional groups present in the synthesized CuO NPs. The FT-IR spectra of

https://doi.org/10.1021/acsomega.3c10179
ACS Omega 2024, 9, 30190−30204

Table 2. XRD Data and Calculation of the Average Size of Synthesized CuO NPs

s. no.	K	λ (Å)	peak position, 2θ (deg)	fwhm, β (deg)	D (nm)
1	0.94	1.54178	32.57	0.34836	24.8
2	0.94	1.54178	35.59	0.45468	19.2
3	0.94	1.54178	38.83	0.58891	14.9
4	0.94	1.54178	48.88	0.55477	16.4
5	0.94	1.54178	53.56	0.60537	15.4
6	0.94	1.54178	58.4	0.64037	14.8
7	0.94	1.54178	61.65	0.64624	14.9
8	0.94	1.54178	66.22	1.1365	8.7
9	0.94	1.54178	68.1	0.7167	13.9
average crystalline size					15.8 nm

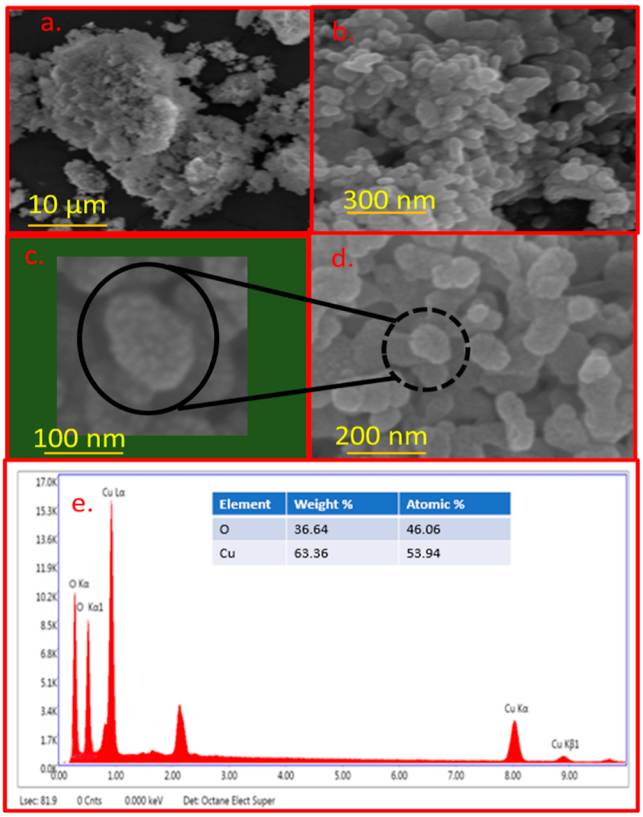

Figure 3. (a−d) SEM micrographs of the synthesized CuO NPs at different resolutions. (e) EDX spectrum of the synthesized CuO NPs.

Table 3. Zeta Potential of CuO NPs and the Average Value of Zeta Potential at 25 °C

s. no.	temperature (°C)	zeta potential (mV)
1	25	−31.2
2	25	−33.8
3	25	−33.5
4	25	−32.8
mean value	25	−32.8

CuO NPs are presented in Figure 2a, showing characteristic peaks at 528, 598, 835, 1021, 1384, 1614, and 3450 cm^{-1}, respectively.[52,53] A weak peak was observed at 3450 cm^{-1}, which can be ascribed to H−O−H bending and −OH stretching vibrations that can be due to the presence of atmospheric water during analysis.[26] A sharp peak at 1614 cm^{-1} corresponded to C═O stretching. The peak at 1384 cm^{-1} was correlated to the sp^3 C−H bending or acyl C−O (or phenol C−O) stretching.[54] The peaks at 1021 and 835 cm^{-1} were allocated to C−O and C−H bending. The characteristic peaks at 527 and 598 cm^{-1}, respectively, indicated the formation of Cu−O stretching vibrations, confirming the formation of CuO NPs.[55] From the FT-IR analysis, the formation of CuO NPs indicated that the phytochemicals present in the aqueous extract were responsible for reducing and stabilizing the metal ions.[56]

3.2. XRD Spectrum of the Synthesized CuO NPs. The XRD spectrum is shown in Figure 2b. The peaks at 32.57, 35.59, 38.84, 48.88, 53.56, 58.40, 61.65, 66.22, and 68.10° were allocated to the planes, viz., (1 1 0), (−1 1 1), (1 1 1), (−2 0 2), (1 1 2), (2 0 2), (−1 1 3), (0 2 2), and (2 2 0), respectively.[57] All the peak points established the monoclinic phase of CuO NPs following the JCPDS card no. (48-1548), which were in agreement with the previous literature.[58,59] The pointed and fine diffraction patterns of the peaks established the fine crystalline nature of the NPs. The mean crystallite size (D) of the CuO NPs was calculated using the Debye−Scherrer eq 2.[60]

$$D = \frac{K\lambda}{\beta \cos\theta} \tag{2}$$

where K = 0.94 is the Scherrer constant. λ = incident X-ray wavelength of 1.542 Å. β = full width at half-maximum (fwhm) of the diffraction peak. θ = diffraction angle.

The calculated average crystallite size (D) was approximately 15.8 nm, as shown in Table 2. No apparent impurity was obtained in the XRD pattern, suggesting high purity of the NPs.

3.3. Optical Properties. The UV−vis spectrum of the CuO NPs was recorded between 200 and 800 nm, as shown in Figure 2c. The absorption spectrum showed maximum absorbance (λ_{max}) at 248 nm, which was attributed to the interband transition of electrons and the fluctuation of surface conduction electrons, which can get excited from one energy level to another upon the incidence of electromagnetic radiation on the surface of the NPs.[61,62] The optical bandgap was calculated from the Tauc's plot using eq 3[63]

$$h\nu \cdot \alpha = (Ah\nu - E_g)^{n/2} \tag{3}$$

Equation 3 can also be transformed into the Kubelka−Munk function form:

The band gap was measured by plotting $(\alpha h\nu)^2$ versus the energy of incident photons ($E = h\nu$), as shown in Figure 2d. The energy gap (E_g) of 3.77 eV was obtained for the CuO NPs, which indicated quantum confinement for the NPs due to their changed morphologies, surface structure, and particle size.[64] The band gap of the CuO NPs can be attributed to their better absorption in the UV region, which may also influence their catalytic activity. The blue-shift behavior of the peak position in comparison with that of the bulk CuO could be attributed to the enhancement of the quantum confinement effect due to the change in size upon formulation. The optical band gap for CuO NPs was much higher than that for bulk CuO (1.85 eV). It has been observed that the UV−vis spectrum of CuO NPs gets shifted to a lower wavelength (blueshift) and higher intensity with a rise in band gap value.[65]

3.4. Morphological Features of the Synthesized CuO NPs. The surface morphology and surface composition of the

https://doi.org/10.1021/acsomega.3c10179
ACS Omega 2024, 9, 30190−30204

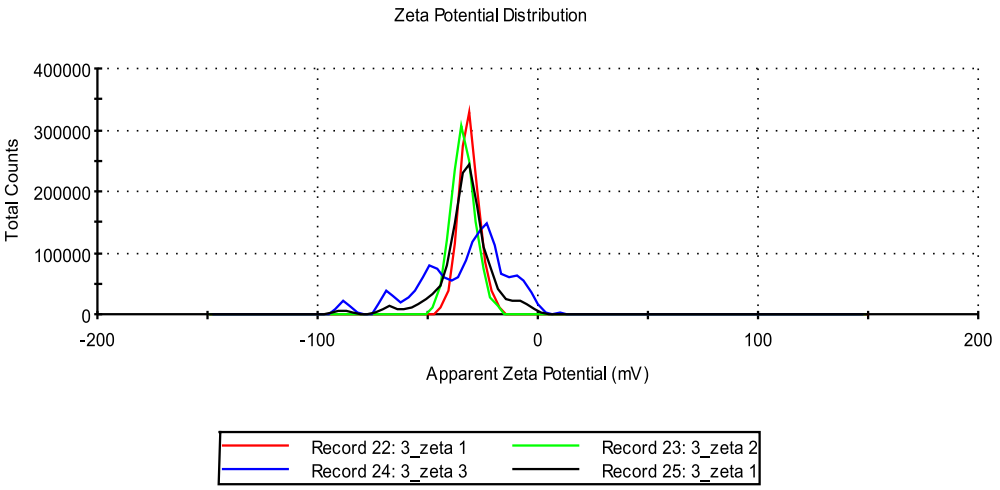

Figure 4. Zeta potential of the CuO NPs.

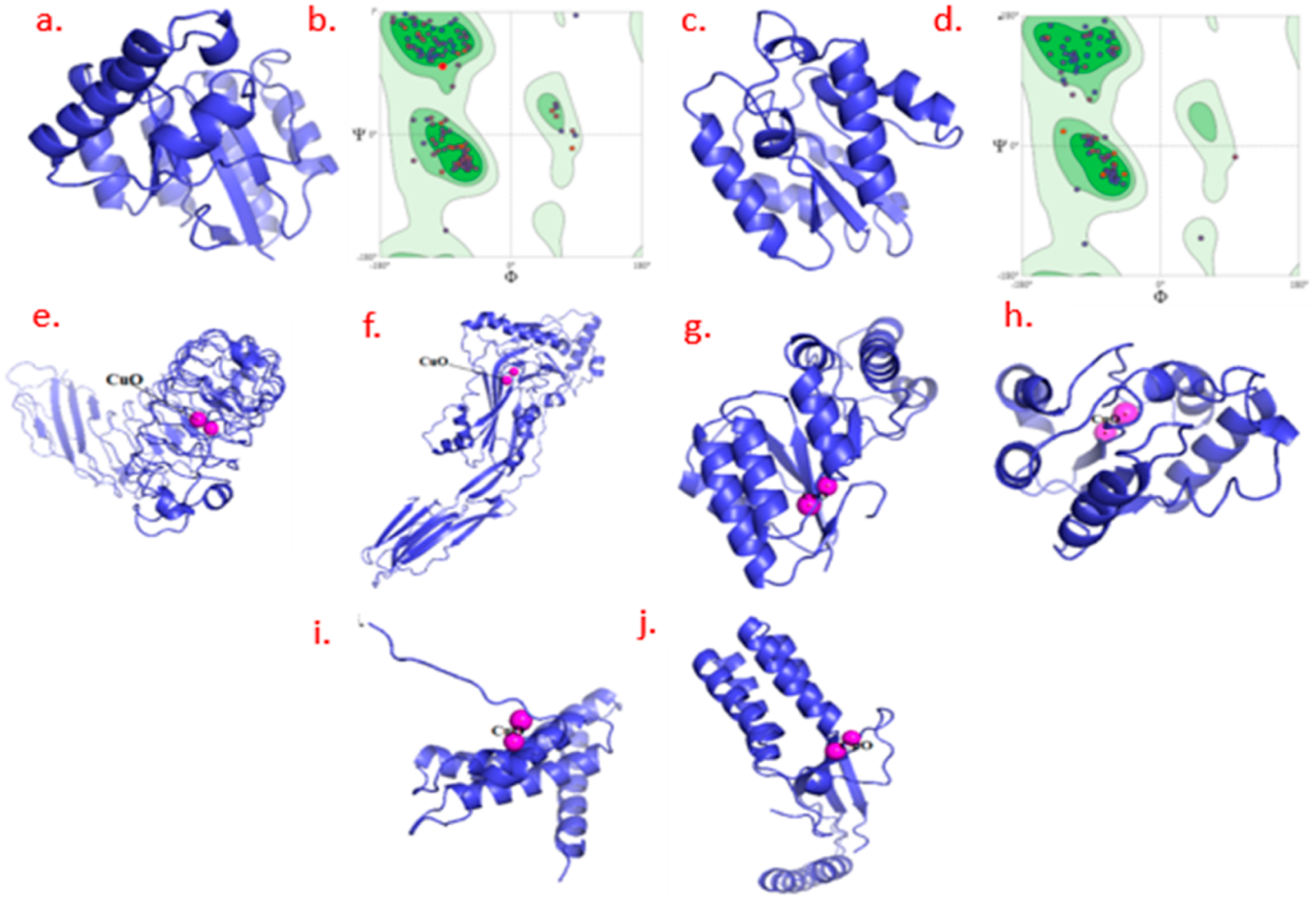

Figure 5. (a) Modeled structure of PgdA, (b) Ramachandran plot for the structural assessment of the modeled PgdA, (c) modeled structure of OatA, (d) Ramachandran plot for the structural assessment of the modeled OatA; CuO NPs docked with target proteins, (e) internalin (InlA) (1O6T), (f) listeriolysin O (PDB ID: 4CDB), (g) PgdA, (h) OatA; docked CuO NPs with the target proteins, (i) SopB, and (j) YfdX.

NPs can be studied by electron microscopy. The morphology and chemical composition of the CuO NPs were determined through FESEM and EDX analysis. The FESEM images of the NPs revealed their sago-shaped structure (Figure 3a–d). The EDX spectrum showed a very consistent copper-rich nanostructure, as shown in Figure 3e. The weight percentage of Cu and O obtained by EDX analysis confirmed the presence of Cu and O. The results were found to be consistent with the literature.[66]

3.5. Zeta Potential. The zeta potential can be considered to be a measure of the valence of the NPs. When NPs are dispersed in water, they tend to stick together due to van der Waals forces. However, if they acquire a charge after dispersing, aggregation can be prevented if the electrostatic repulsion overcomes the van der Waals force.[67] The zeta

https://doi.org/10.1021/acsomega.3c10179
ACS Omega 2024, 9, 30190−30204

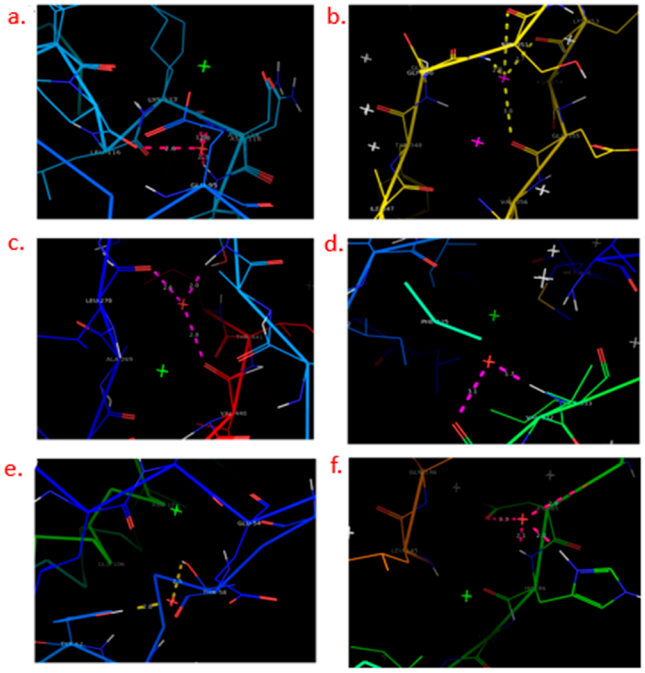

Figure 6. Interaction of the synthesized CuO NPs with (a) internalin (InlA) (1O6T), (b) listeriolysin O, (c) PgdA, (d) OatA, (e) SopB, and (f) YfdX.

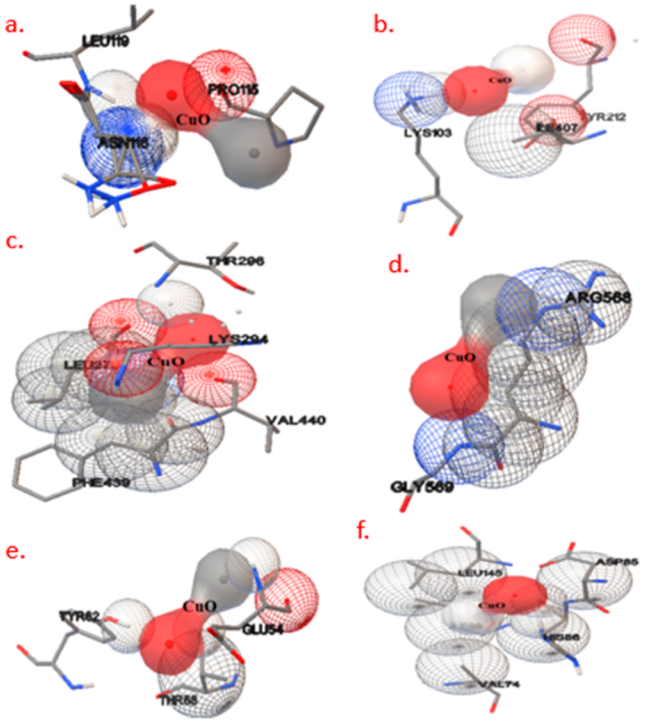

Figure 7. Interacting residues of target proteins with (a) internalin (InlA), (b) listeriolysin O, (c) PgdA, (d) OatA, (e) SopB, and (f) YfdX.

potential of the synthesized NPs was found to be −32.8 mV (Table 3 and Figure 4).

3.6. Molecular Docking Studies. The modeled structure of PgdA showed the highest sequence identity of 44.67% with *Streptococcus pneumoniae* peptidoglycan deacetylase (PDB ID: 2C1G), and it served as the template for the modeling of PgdA. The protein OatA modeled structure showed the highest sequence identity of 49.31% with the structure of *S. aureus* peptidoglycan OatA C-terminal catalytic domain (PDB ID: 6VJP), and it is served as a template for the modeling of OatA. For both modeled proteins, the sequence identity was more than 40%, making them suitable for further consideration.[68] The GMQE and QMEAN values for PgdA were 0.32 and −1.57, while for OatA, they were 0.18 and −0.37, which further suggested the reliability of the modeled structures. The Ramachandran plot (Figure 5) obtained for modeled PgdA and OatA have the Ramachandran favored region 95.38% for PgdA and 95.77% for OatA modeled proteins. The interactions of CuO NPs with the residues of the target proteins are shown in Figures 6 and 7. The docking score of CuO NP's interaction with target proteins is presented in Tables 4 and 5, along with the interacting residues.

Table 4. Docking Score of CuO NPs with the Target Protein of *L. monocytogenes*

s. no.	target protein with PDB ID	docking score (kcal/mol)	interacting residues
1	internalin (InlA) (1O6T)	−2.53	LEU119, PRO115, ASN116
2	listeriolysin O (4CDB)	−2.07	LYS103, TYR212, ILE407
3	PgdA	−2.02	THR296, LYS296, VAL440, PHE439, LEU227
4	OatA	−2.02	ARG568, GLY569

Table 5. Docking Score of CuO NPs with the Target Protein of *S. typhi*

s. no.	target protein with PDB ID	docking score (kcal/mol)	interacting residues
1	SopB (4DID)	−2.04	TYR62, THR56, GLU64
2	YfdX (6A07)	−2.01	LEU145, ASP85, HIS86, VAL74

The docking analysis suggested that the CuO NPs interacted with target proteins of both *Listeria monocytogenes* and *S. typhi*. *L. monocytogenes* showed the best docking score against internalin (InlA) with a binding energy of −2.53 kcal/mol, while *S. typhi* targets SopB (PDB ID: 4DID) showed the best docking score of −2.04 kcal/mol. It is very important to comprehend the protein−metal binding and the complex formed during the interaction between nanomaterials and the biomolecules and that has led to the utility of molecular docking, which predicts the cooperation affinity of the protein−metal complex and also the hindrances and limitations where the binding is not feasible.[69] For the biomedical applications of nanomaterials, the applications of molecular docking are numerous yet under-explored.

3.7. Antibacterial Activity of the Synthesized CuO NPs. The antibacterial activity assessment of CuO NPs was done by comparing the growth of inhibition zones to the standard antibiotic streptomycin. DMSO was taken as a negative control, which did not show any effect on the bacterial pathogens. The efficiency of the CuO NPs in the treatment of the bacterial strains was noteworthy ($p < 0.0001$), and the width of the developed inhibitory zones broadened with the rise in the concentration of the CuO NPs, as depicted in Table 6. The minimum inhibitory concentration (MIC) and minimum bactericidal concentration (MBC) were also calculated. MIC depicted the lowest concentration of the compound restricting bacterial growth (Table 7). CuO NPs

https://doi.org/10.1021/acsomega.3c10179
ACS Omega 2024, 9, 30190−30204

Table 6. Zone of Inhibition (mm) of the CuO NPs

s. no.	compound	zone of inhibition (mm)			
		L. monocytogenes	*K. pneumoniae*	*S. typhi*	*P. aeruginosa*
1	CuO NPs	15 ± 0.04	10 ± 0.04	13 ± 0.02	10 ± 0.08
2	streptomycin	15 ± 0.02	22 ± 0.02	17 ± 0.08	26 ± 0.04

Table 7. MIC and MBC Values of the CuO NPs

s. no.	compound	organisms MIC (μg)			
		L. monocytogenes	*K. pneumoniae*	*S. typhi*	*P. aeruginosa*
1	CuO NPs	256 ± 0.02	512 ± 0.04	256 ± 0.06	256 ± 0.02
2	streptomycin	64 ± 0.06	16 ± 0.02	8 ± 0.02	128 ± 0.08
s. no.	compound	organisms MBC (μg)			
		L. monocytogenes	*K. pneumoniae*	*S. typhi*	*P. aeruginosa*
1	CuO NPs	512 ± 0.02	>512	512 ± 0.02	512 ± 0.02
2	streptomycin	128 ± 0.02	32 ± 0.02	8 ± 0.02	256 ± 0.02

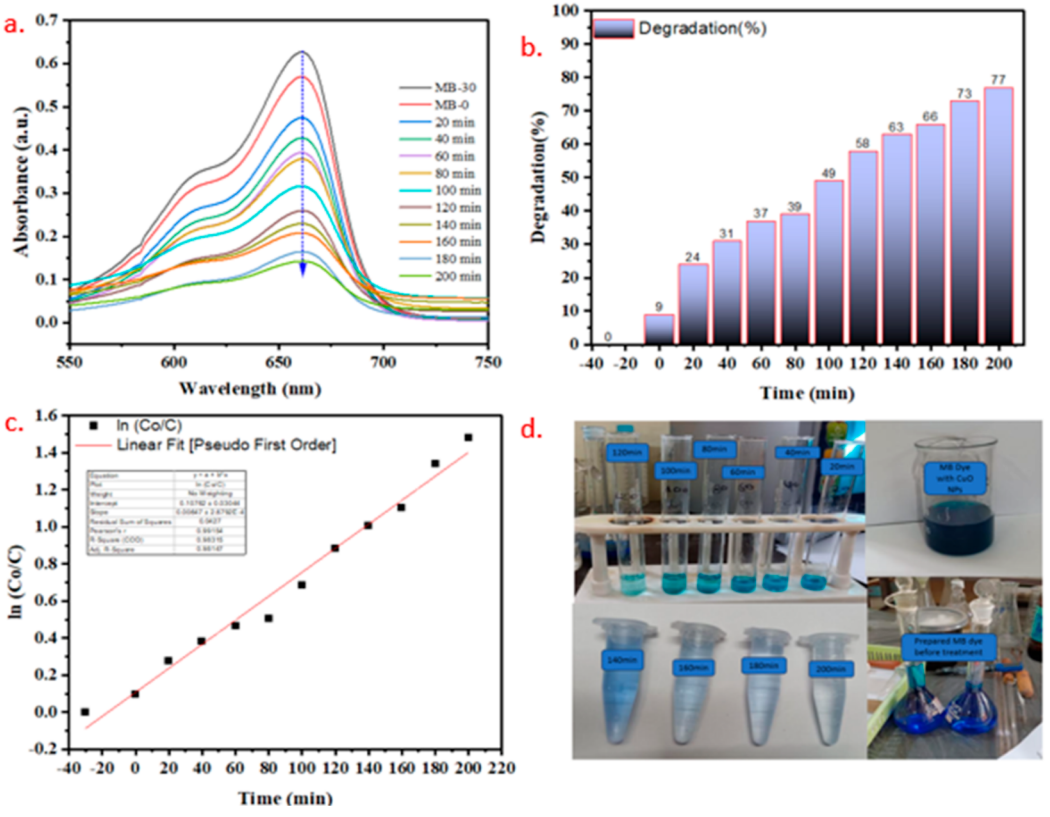

Figure 8. (a) UV−vis spectrum of MB in the presence of the synthesized CuO under UV light irradiation, (b) histogram for the extent of discoloration of MB dye as a function of time, (c) first-order rate kinetics of photodegradation reaction, and (d) color change observed after photocatalysis.

exhibited appreciable activity against the tested bacterial strains. The highest zone of inhibition (15 ± 0.04 mm) was observed against *L. monocytogenes*, followed by *S. typhi* (13 ± 0.02 mm). A previous study reported the antimicrobial activity of CuO NPs fabricated via *A. citrus* extract. The activity was evaluated against *Clostridium perfringens*, *Campylobacter coli*, *E. coli*, *L. monocytogenes*, *S. pneumoniae*, *P. aeruginosa*, and *Moraxella catarrhalis*, of which *S. aureus* and *E. coli* had a significant zone of inhibition as compared to the positive control (tetracycline). The effective antibacterial activity of the green synthesized CuO NPs may be ascribed to the overall negative zeta potential/charge, and it has been suggested that values greater and positive than +30 mV and negative than −30 mV impart stability against amalgamation.[70] The electrostatic interface, adsorption, and subsequent penetration of the bacterial surface by the CuO NPs might have boosted the antibacterial activity. The antibacterial activity of the NPs may also be ascribed to the release of Cu(II) ions, which may get adhered to the bacterial cell wall due to the electrostatic force of attraction. The morphology of the nanostructure may also play a role in its overall assessment. The novel sago-shaped NPs possessed a high surface area to volume ratio that might have improved their interface with the bacterial cells, thereby obstructing their growth. Smaller NPs (less than 30 nm) are

https://doi.org/10.1021/acsomega.3c10179
ACS Omega 2024, 9, 30190−30204

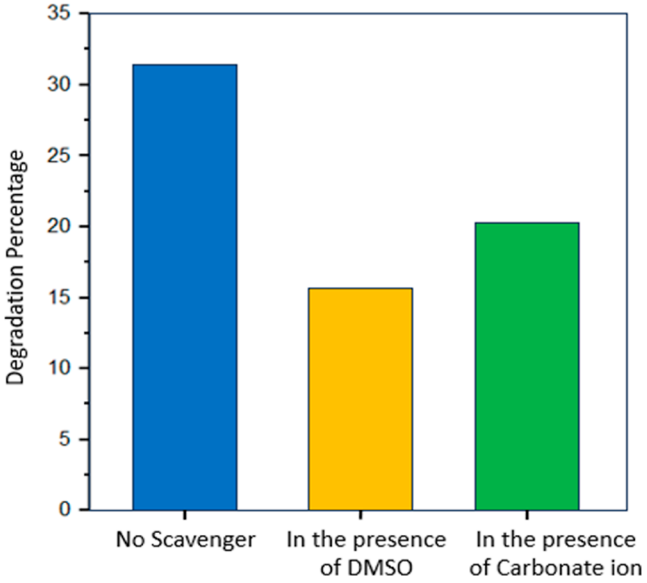

Figure 9. Degradation percentage of MB dye with CuO NPs in the presence of a scavenger.

more likely to penetrate the bacterial cell wall due to the improved surface area/volume ratio.[71] Another mechanism explaining bactericidal activity is the formation of reactive oxygen species (ROS) by the interface with CuO NPs leading to the inhibition of respiratory enzymes and, consequently, the death of the bacterial cell.[72]

3.8. Photocatalytic Activity. The photocatalytic activity of CuO NPs was tested against MB dye under UV light irradiation by measuring the change in the absorption. Figure 8a depicts a time-dependent UV−vis absorption spectrum showing an MB dye reaction-mediated color change under UV light irradiation. A decrease in the absorption peak at 664 nm confirmed the MB dye chromogenic reaction. A significant (≈77%) degradation was observed in 200 min confirming that the CuO NPs may act as an effective photocatalyst. Figure 8b depicts the extent of discoloration of the MB dye. The dye degradation by the sago-shaped CuO NPs may be explained by the charge transfer of the valence band to the electron carrier, which reduces the risk of electron−hole pair recombination.[73]

The kinetics of MB dye degradation followed the Langmuir−Hinshelwood model. The rate eq 4 for Langmuir−Hinshelwood mode is described as

$$\ln\left[\frac{C_0}{C_t}\right] = K_{app}t \tag{4}$$

Among them, C_0 and C_t signify the dye concentration at time "0" and "t", respectively, and "K_{app}" signifies the deceptive pseudo-first-order constant value. Figure 8c reveals a typical first-order kinetics plot of MB dye discoloration reaction, a plot $\ln(C_0/C)$ versus time that gives a straight-line slope, which is equal to the first-order rate constant K_{app} (0.01135 min^{-1}) and regression coefficient R^2 (0.98315), and the result matched well with the earlier reported work.[74] The initial and final colors of the chosen dyes are presented in Figure 8d.

3.8.1. Role of Scavengers on Dye Degradation. To study the qualitative effect, DMSO and carbonate ions were used as scavengers for chemically active species. To carry out the experiment, the concentration of CuO NPs taken was 0.4 g/L and the concentration of DMSO or carbonate ion taken was 0.3 g/L in 100 mL of dye solution. The reaction mixture was irradiated with UV−visible radiation for 60 min. It was observed that in the absence of a scavenger (DMSO or carbonate ion), percentage degradation of dye was 33.7% but when DMSO or carbonate ion was added to the dye solution, the percentage degradation of dye decreased to 15.6 and 19.5%, respectively (Figure 9). From the experimental results, it was concluded that the concentration of active radicals that are responsible for the degradation decreased in the presence of scavengers. The scavenging mechanism is shown by eqs 5 and 6[75]

$$OH^{\bullet} + (CH_3)_2SO \rightarrow CH_3^{\bullet} + CH_3SO_2H \tag{5}$$

$$OH^{\bullet} + CO_3^{2-} \rightarrow OH^{-} + CO_3^{-} \tag{6}$$

3.8.2. Effect of Material Dose. The concentration of the CuO NPs may affect the percentage of degradation of the dye. In Figure 10a,b, it can be observed that the percentage degradation of dye increased with the increase in the

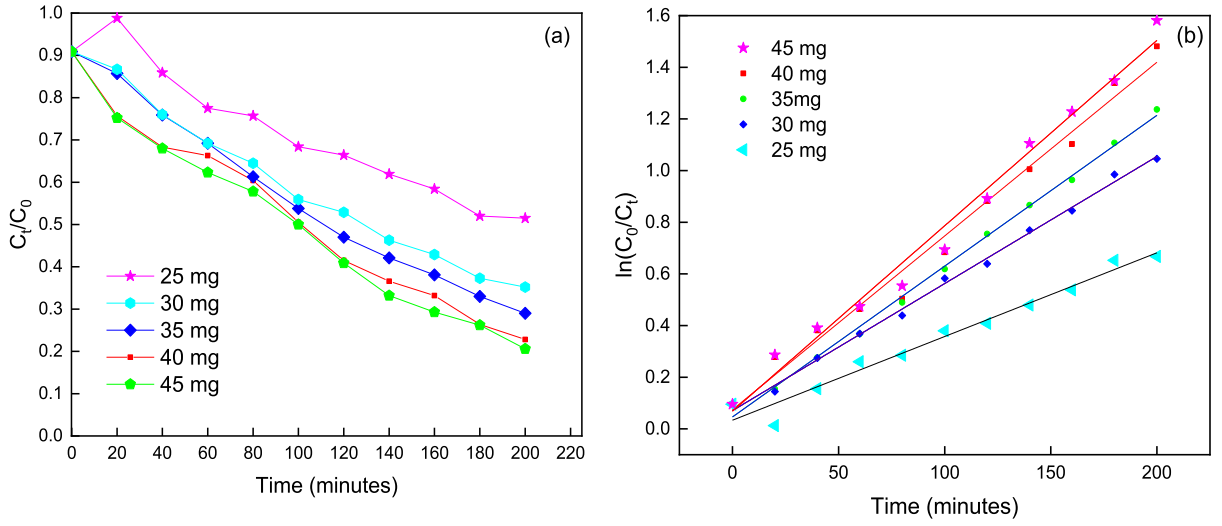

Figure 10. (a,b) Dose-dependent effect of the synthesized CuO NPs on MB dye.

https://doi.org/10.1021/acsomega.3c10179
ACS Omega 2024, 9, 30190−30204

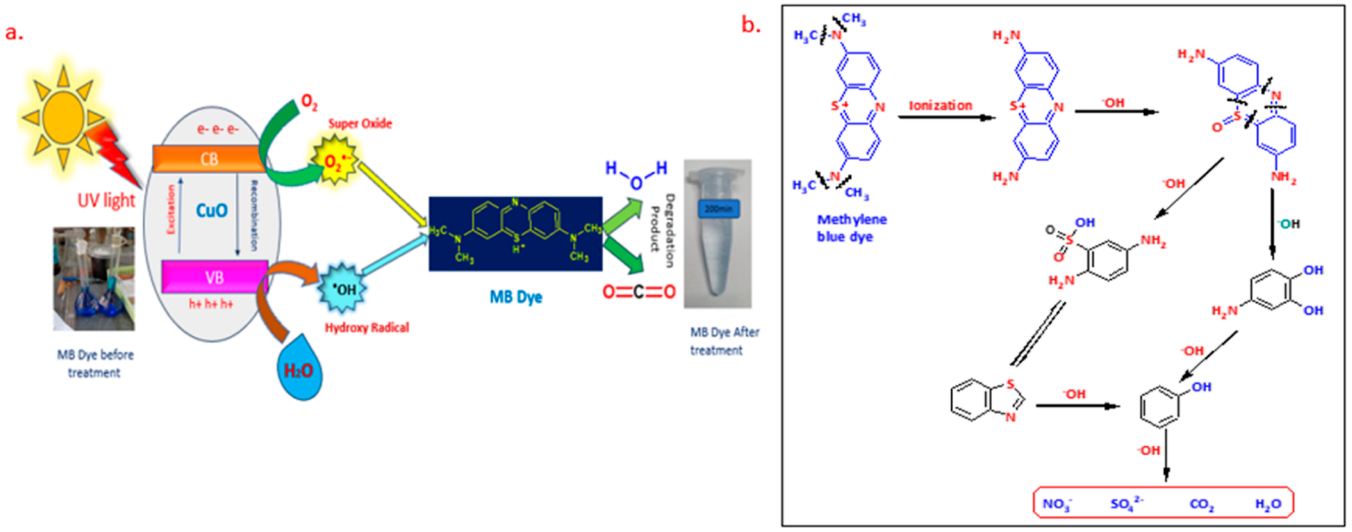

Figure 11. (a) Plausible mechanism of dye degradation of synthesized CuO NPs and (b) proposed mechanism of degradation of MB dye.

Table 8. Comparative Assessment of the Dye Degradation by Metal Oxide-Based NPs

catalyst system	dye used	degradation	preparation method	light source used	refs
Fe, Co, Ni, Cu, and Zn−TiO_2	AB92	DE (90%), Fe−TiO_2 (80%), Co−TiO_2 (12%), Ni−TiO_2 (8%), Zn−TiO_2 (20%)	sol−gel method	UV light	79
CuO and CeO_2/CuO	MB	33.4 and 70.1%	thermal decomposition	visible light	81
ZnO NPs	rhodamine B	70%	green synthesis	UV light	82
TiO_2	MB	71%	green synthesis	UV light	83
CuO/ZnO	MB	73%	green microwave-assisted method	UV light	84
CuO and CuO−GO nanocomposite	MB	75 and 83.20%	green synthesis	visible light	85
Cu_2O- and CuO-NP	MB	70 and 63	chemical method	sun light	86
Ni−CuO, Zn−CuO, Fe−CuO	MB	52, 63, 62%	sonication method	500 W xenon lamp	87
CuO	MO	45.23%	green synthesis	UV light	88
Cu_2O	MB	70%	green synthesis	UV light	89
G−ZnO composite	MB	68.6%	ESD technique	UV light	90
CuO	MB	77%	green synthesis	UV light	**present work**

concentration of CuO NPs from 25 to 40 mg. However, a further increase in CuO NPs from 40 to 45 mg had a negligible effect on the degradation of dye. Therefore, 40 mg of CuO NPs in 100 mL of dye solution was found to be the optimum amount. This increase in the percentage degradation of dye may be because the active sites increase with the increase in CuO NP dosage.

3.8.3. Dye Degradation Mechanism. The valence state and conduction band edge potential of the prepared nano-photocatalyst were used to study the photocatalytic process, and the following eq 7 can be used to predict the E_{VB} of the prepared process

$$E_{VB} = X - E^e + 0.5E_g \quad (7)$$

X represents the electronegativity of the material atoms, E_g represents the energy difference, and E^e represents the energy of free electrons. The E_{CB} of the catalyst was determined by eq 8

$$E_{CB} = E_{VB} - E_g \quad (8)$$

Therefore, the value of the valence band of CuO was calculated to be +0.70 eV and the conduction band value was −1.03.[76] Figure 11a depicts the detailed mechanism of the color change reaction. As photons with suitable wavelengths are irradiated on the NPs, they cause excitation and electron−hole (e^-/h^+) pair formation. Electrons from the conduction band roam to the surface of the CuO NPs and are swept away by the ubiquitous O_2, forming the superoxide anion O_2^{2-}. Upon protonation, $HOO^\bullet$ radicals are produced, which further react with the electrons to form H_2O_2. At the same time, h^+ in the valence band moves to the back of the CuO NPs' surface and reacts with H_2O/OH^- and dye molecules to form OH and OH^- (eqs 9−14)

$$CuO + h\nu \rightarrow CuO(e^-_{CB} + h^+_{VB}) \quad (9)$$

$$e^-_{CB} + O_2 \rightarrow O_2^{\bullet-} + H^+ \rightarrow HOO^\bullet \quad (10)$$

$$h^+_{VB} + H_2O \rightarrow {}^\bullet OH + H^+ \quad (11)$$

$$HOO^\bullet + e^-_{CB} + H^+ \rightarrow H_2O_2 \quad (12)$$

https://doi.org/10.1021/acsomega.3c10179
ACS Omega 2024, 9, 30190−30204

$$H_2O_2^{\bullet} + e_{CB}^{-} + H^{+} \rightarrow {}^{\bullet}OH + OH^{-} \quad (13)$$

$$({}^{\bullet}OH, O_2^{\bullet -}) + \text{dye} \rightarrow \text{degradation products} \quad (14)$$

The degradation initiates with the contravention of the C−S^{+}=C bond from the MB dye functional group, which facilitates the whole conversion of nitrogen, carbon, and sulfur hetero atoms into CO_2, NO_3^{-}, SO_4^{2-}, and H_2O mineralization ions, as depicted in Figure 11b. The overall reaction can be summarized in eq 15[77]

$$C_{16}H_{18}N_3S^{+} + 102OH + \text{UV light} \rightarrow 16CO_2 + 3NO_3^{-} + SO_4^{2-} + 6H^{+} + 57H_2O \quad (15)$$

Therefore, the development of highly ROS {O_2, OH^{-} or $HOO^{\bullet}$} is responsible for the mineralization of MB dyes to harmless products. If the photogenerated e^{-}/h^{+} pair cannot reach the active surface, they recombine, which is the key reason for the photodegradation efficiency to decrease. Therefore, the movement of electrons from the valence band to the conduction band will determine the efficiency of the photodegradation reaction.[78] As the photocatalytic reaction is fixed on the catalyst surface, the above process and morphological results justify that the green synthesized CuO NPs grow uniformly and densely and have high crystallinity, which is good for photoexcitation of carriers and reduces recombination chances. MB decay results confirm that CuO is an effective photocatalyst under UV light irradiation (Table 8).[80]

4. CONCLUSIONS

The present study reported the green synthesis of CuO NPs from the plant extract of *A. vera*. Although the medicinal properties of the plant and NPs fabricated from the plant extract are well-documented, there is always scope for improvement and new features in the existing literature. The synthesized CuO NPs were found to have a novel sago shape. They were also obtained in an appreciable yield even at 70−80 °C, and the size was well below 20 nm. Furthermore, docking studies and homology modeling were also performed to gain insight into the binding interactions between the NPs and the selected proteins. The photocatalytic activity was also added to the utility of the synthesized environment-friendly NPs. A thorough comparison was also made with previous studies in terms of reaction conditions and studied applications. In the future, the docking results can be elaborated through molecular dynamics simulations to comprehend a deeper understanding of the interface between the target and the ligand. They should also be studied for other medicinal applications. Furthermore, owing to their morphological features and appreciable zeta potential value, they can also be explored for diverse applications.

AUTHOR INFORMATION

Corresponding Authors

Vasi Uddin Siddiqui − *Advanced Engineering Materials and Composites Research Centre (AEMC), Department of Mechanical and Manufacturing Engineering, Universiti Putra Malaysia, UPM, Serdang, Selangor Darul Ehsan 43400, Malaysia*; orcid.org/0000-0003-3427-8943; Email: vasi.siddiqui@gmail.com

Tahmeena Khan − *Department of Chemistry, Integral University, Lucknow 226026 Uttar Pradesh, India*; Email: tahminakhan30@yahoo.com

Authors

Sabeeha Jabeen − *Department of Chemistry, Integral University, Lucknow 226026 Uttar Pradesh, India; Department of Chemistry, University of Lucknow, Lucknow 226007 Uttar Pradesh, India*

Shashi Bala − *Department of Chemistry, University of Lucknow, Lucknow 226007 Uttar Pradesh, India*

Nidhi Mishra − *Department of Applied Sciences, Indian Institute of Information Technology, Allahabad 2110155 Uttar Pradesh, India*; orcid.org/0000-0002-6028-7723

Anamika Mishra − *Department of Applied Sciences, Indian Institute of Information Technology, Allahabad 2110155 Uttar Pradesh, India*

Rubina Lawrence − *Department of Industrial Microbiology, Sam Higginbottom University of Agriculture Technology and Sciences, Allahabad 211007 Uttar Pradesh, India*

Pratibha Bansal − *Department of Chemistry, University of Lucknow, Lucknow 226007 Uttar Pradesh, India*

Abdul Rahman Khan − *Department of Chemistry, Integral University, Lucknow 226026 Uttar Pradesh, India*

Complete contact information is available at: https://pubs.acs.org/10.1021/acsomega.3c10179

Notes

The authors declare no competing financial interest.

ACKNOWLEDGMENTS

The authors acknowledge the R&D cell of Integral University, Lucknow, for providing the manuscript communication number IU/R&D/2023-MCN0001813.

REFERENCES

(1) Mondal, P.; Anweshan, A.; Purkait, M. K. Green Synthesis and Environmental Application of Iron-Based Nanomaterials and Nanocomposite: A Review. *Chemosphere* **2020**, *259*, 127509.

(2) Akintelu, S. A.; Oyebamiji, A. K.; Olugbeko, S. C.; Folorunso, A. S. Green Synthesis of Iron Oxide Nanoparticles for Biomedical Application and Environmental Remediation: A Review. *Ecletica Quim.* **2021**, *46* (4), 17−37.

(3) Arun Paul, C.; Ranjith Kumar, E.; Abd El-Rehim, A. F.; Yang, G. Cobalt Oxide Nanoparticles for Biological Applications: Synthesis and Physicochemical Characteristics for Different Natural Fuels. *Ceram. Int.* **2023**, *49* (24), 40244−40257.

(4) Liu, Q.; Zhang, A.; Wang, R.; Zhang, Q.; Cui, D. A Review on Metal- and Metal Oxide-Based Nanozymes: Properties, Mechanisms, and Applications. *Nano-Micro Lett.* **2021**, *13* (1), 154.

(5) Repko, A.; Vejpravová, J.; Vacková, T.; Zákutná, D.; Nižňanský, D. Oleate-Based Hydrothermal Preparation of CoFe2O4 Nanoparticles, and Their Magnetic Properties with Respect to Particle Size and Surface Coating. *J. Magn. Magn. Mater.* **2015**, *390* (390), 142−151.

(6) Kirillov, V. L.; Balaev, D. A.; Semenov, S. V.; Shaikhutdinov, K. A.; Martyanov, O. N. Size Control in the Formation of Magnetite Nanoparticles in the Presence of Citrate Ions. *Mater. Chem. Phys.* **2014**, *145* (1−2), 75−81.

(7) Gahrouei, Z. E.; Imani, M.; Soltani, M.; Shafyei, A. Synthesis of Iron Oxide Nanoparticles for Hyperthermia Application: Effect of Ultrasonic Irradiation Assisted Co-Precipitation Route. *Adv. Nat. Sci. Nanosci. Nanotechnol.* **2020**, *11* (2), 025001.

(8) Sonkusare, V. N.; Chaudhary, R. G.; Bhusari, G. S.; Mondal, A.; Potbhare, A. K.; Mishra, R. K.; Juneja, H. D.; Abdala, A. A.

Mesoporous Octahedron-Shaped Tricobalt Tetroxide Nanoparticles for Photocatalytic Degradation of Toxic Dyes. *ACS Omega* **2020**, *5* (14), 7823−7835.
(9) Su, B.; Lin, J.; Owens, G.; Chen, Z. Impact of Green Synthesized Iron Oxide Nanoparticles on the Distribution and Transformation of As Species in Contaminated Soil. *Environ. Pollut.* **2020**, *258*, 113668.
(10) Hosseini-Koupaei, M.; Shareghi, B.; Saboury, A. A.; Davar, F.; Sirotkin, V. A.; Hosseini-Koupaei, M. H.; Enteshari, Z. Catalytic Activity, Structure and Stability of Proteinase K in the Presence of Biosynthesized CuO Nanoparticles. *Int. J. Biol. Macromol.* **2019**, *122*, 732−744.
(11) Jan, H.; Shah, M.; Usman, H.; Khan, M. A.; Zia, M.; Hano, C.; Abbasi, B. H. Biogenic Synthesis and Characterization of Antimicrobial and Antiparasitic Zinc Oxide (ZnO) Nanoparticles Using Aqueous Extracts of the Himalayan Columbine (Aquilegia Pubiflora). *Front. Mater.* **2020**, *7* (August), 1−14.
(12) Berra, D.; Salah Eddine, L.; Boubaker, B.; Ridha, O. M.; Berra, D.; Laouini, S. E.; Benhaoua, B.; Ouahrani, M. R.; Berrani, D.; Rahal, A. Green Synthesis of Copper Oxide Nanoparticles By Pheonix Dactylifera L Leaves Extract. *Dig. J. Nanomater. Biostruct.* **2018**, *13* (4), 1231−1238.
(13) Nagajyothi, P. C.; Pandurangan, M.; Kim, D. H.; Sreekanth, T. V. M.; Shim, J. Green Synthesis of Iron Oxide Nanoparticles and Their Catalytic and In Vitro Anticancer Activities. *J. Cluster Sci.* **2017**, *28* (1), 245−257.
(14) Karpagavinayagam, P.; Vedhi, C. Green Synthesis of Iron Oxide Nanoparticles Using Avicennia Marina Flower Extract. *Vacuum* **2019**, *160*, 286−292.
(15) Arularasu, M. V.; Devakumar, J.; Rajendran, T. V. An Innovative Approach for Green Synthesis of Iron Oxide Nanoparticles: Characterization and Its Photocatalytic Activity. *Polyhedron* **2018**, *156*, 279−290.
(16) Subhapriya, S.; Gomathipriya, P. Green Synthesis of Titanium Dioxide (TiO2) Nanoparticles by Trigonella Foenum-Graecum Extract and Its Antimicrobial Properties. *Microb. Pathog.* **2018**, *116*, 215−220.
(17) Sone, B. T.; Diallo, A.; Fuku, X. G.; Gurib-Fakim, A.; Maaza, M. Biosynthesized CuO Nano-Platelets: Physical Properties & Enhanced Thermal Conductivity Nanofluidics. *Arab. J. Chem.* **2020**, *13* (1), 160−170.
(18) Umar, A.; Ibrahim, A. A.; Nakate, U. T.; Albargi, H.; Alsaiari, M. A.; Ahmed, F.; Alharthi, F. A.; Ali Alghamdi, A.; Al-Zaqri, N. Fabrication and Characterization of CuO Nanoplates Based Sensor Device for Ethanol Gas Sensing Application. *Chem. Phys. Lett.* **2021**, *763*, 138204.
(19) Rajendaran, K.; Muthuramalingam, R.; Ayyadurai, S. Green Synthesis of Ag-Mo/CuO Nanoparticles Using Azadirachta Indica Leaf Extracts to Study Its Solar Photocatalytic and Antimicrobial Activities. *Mater. Sci. Semicond. Process.* **2019**, *91*, 230−238.
(20) Mohamed, A. A.; Abu-Elghait, M.; Ahmed, N. E.; Salem, S. S. Eco-Friendly Mycogenic Synthesis of ZnO and CuO Nanoparticles for In Vitro Antibacterial, Antibiofilm, and Antifungal Applications. *Biol. Trace Elem. Res.* **2021**, *199* (7), 2788−2799.
(21) Mahmood, R. I.; Kadhim, A. A.; Ibraheem, S.; Albukhaty, S.; Mohammed-Salih, H. S.; Abbas, R. H.; Jabir, M. S.; Mohammed, M. K. A.; Nayef, U. M.; AlMalki, F. A.; Sulaiman, G. M.; Al-Karagoly, H. Biosynthesis of Copper Oxide Nanoparticles Mediated Annona Muricata as Cytotoxic and Apoptosis Inducer Factor in Breast Cancer Cell Lines. *Sci. Rep.* **2022**, *12* (1), 16165.
(22) Saha, T.; Bin Mobarak, M.; Uddin, M. N.; Quddus, M. S.; Naim, M. R.; Pinky, N. S. Biogenic Synthesis of Copper Oxide (CuO) NPs Exploiting Averrhoa Carambola Leaf Extract and Its Potential Antibacterial Activity. *Mater. Chem. Phys.* **2023**, *305*, 127979.
(23) Potbhare, A. K.; Chaudhary, R. G.; Chouke, P. B.; Yerpude, S.; Mondal, A.; Sonkusare, V. N.; Rai, A. R.; Juneja, H. D. Phytosynthesis of Nearly Monodisperse CuO Nanospheres Using Phyllanthus Reticulatus/Conyza Bonariensis and Its Antioxidant/Antibacterial Assays. *Mater. Sci. Eng., C* **2019**, *99*, 783−793.
(24) Ettadili, F. E.; Aghris, S.; Laghrib, F.; Farahi, A.; Saqrane, S.; Bakasse, M.; Lahrich, S.; El Mhammedi, M. A. Recent Advances in the Nanoparticles Synthesis Using Plant Extract: Applications and Future Recommendations. *J. Mol. Struct.* **2022**, *1248*, 131538.
(25) Abo-zeid, Y.; Ismail, N. S. M.; McLean, G. R.; Hamdy, N. M. A Molecular Docking Study Repurposes FDA Approved Iron Oxide Nanoparticles to Treat and Control COVID-19 Infection. *Eur. J. Pharm. Sci.* **2020**, *153*, 105465.
(26) Chouke, P. B.; Potbhare, A. K.; Meshram, N. P.; Rai, M. M.; Dadure, K. M.; Chaudhary, K.; Rai, A. R.; Desimone, M. F.; Chaudhary, R. G.; Masram, D. T. Bioinspired NiO Nanospheres: Exploring In Vitro Toxicity Using Bm-17 and L. Rohita Liver Cells, DNA Degradation, Docking, and Proposed Vacuolization Mechanism. *ACS Omega* **2022**, *7* (8), 6869−6884.
(27) Raizada, P.; Sudhaik, A.; Patial, S.; Hasija, V.; Parwaz Khan, A. A.; Singh, P.; Gautam, S.; Kaur, M.; Nguyen, V.-H. Engineering Nanostructures of CuO-Based Photocatalysts for Water Treatment: Current Progress and Future Challenges. *Arab. J. Chem.* **2020**, *13* (11), 8424−8457.
(28) Kayalvizhi, S.; Sengottaiyan, A.; Selvankumar, T.; Senthilkumar, B.; Sudhakar, C.; Selvam, K. Eco-Friendly Cost-Effective Approach for Synthesis of Copper Oxide Nanoparticles for Enhanced Photocatalytic Performance. *Optik* **2020**, *202*, 163507.
(29) Singh, J.; Kumar, V.; Kim, K.-H.; Rawat, M. Biogenic Synthesis of Copper Oxide Nanoparticles Using Plant Extract and Its Prodigious Potential for Photocatalytic Degradation of Dyes. *Environ. Res.* **2019**, *177*, 108569.
(30) Mohammed Yusuf Ansari, P.; Muthukrishnan, R. M.; Imran Khan, R.; Vedhi, C.; Sakthipandi, K.; Abdul Kader, S. M. Green Synthesis of Copper Oxide Nanoparticles Using Amaranthus Dubius Leaf Extract for Sensor and Photocatalytic Applications. *Chem. Phys. Impact* **2023**, *7*, 100374.
(31) Javid-Naderi, M. J.; Sabouri, Z.; Jalili, A.; Zarrinfar, H.; Samarghandian, S.; Darroudi, M. Green Synthesis of Copper Oxide Nanoparticles Using Okra (Abelmoschus Esculentus) Fruit Extract and Assessment of Their Cytotoxicity and Photocatalytic Applications. *Environ. Technol. Innovat.* **2023**, *32*, 103300.
(32) Sánchez-Machado, D. I.; López-Cervantes, J.; Sendón, R.; Sanches-Silva, A. Aloe Vera: Ancient Knowledge with New Frontiers. *Trends Food Sci. Technol.* **2017**, *61*, 94−102.
(33) Hęś, M.; Dziedzic, K.; Górecka, D.; Jędrusek-Golińska, A.; Gujska, E. Aloe Vera (L.) Webb.: Natural Sources of Antioxidants - A Review. *Plant Foods Hum. Nutr.* **2019**, *74* (3), 255−265.
(34) Rafique, M.; Shaikh, A. J.; Rasheed, R.; Tahir, M. B.; Gillani, S. S. A.; Usman, A.; Imran, M.; Zakir, A.; Khan, Z. U. H.; Rabbani, F. Aquatic Biodegradation of Methylene Blue by Copper Oxide Nanoparticles Synthesized from Azadirachta Indica Leaves Extract. *J. Inorg. Organomet. Polym. Mater.* **2018**, *28* (6), 2455−2462.
(35) Skariyachan, S.; Parveen, A.; Garka, S. Nanoparticle Fullerene (C60) Demonstrated Stable Binding with Antibacterial Potential towards Probable Targets of Drug Resistant Salmonella Typhi - a Computational Perspective and in Vitro Investigation. *J. Biomol. Struct. Dyn.* **2017**, *35* (16), 3449−3468.
(36) Troxell, B.; Sikes, M. L.; Fink, R. C.; Vazquez-Torres, A.; Jones-Carson, J.; Hassan, H. M. Fur Negatively Regulates Hns and Is Required for the Expression of HilA and Virulence in Salmonella Enterica Serovar Typhimurium. *J. Bacteriol.* **2011**, *193* (2), 497−505.
(37) Derakhshan, Z.; Baghapour, M. A.; Ranjbar, M.; Faramarzian, M. Adsorption of Methylene Blue Dye from Aqueous Solutions by Modified Pumice Stone: Kinetics and Equilibrium Studies. *Health Scope* **2013**, *2* (3), 136−144.
(38) Yusuf, L. A.; Ertekin, Z.; Fletcher, S.; Symes, M. D. Enhanced Ultrasonic Degradation of Methylene Blue Using a Catalyst-Free Dual-Frequency Treatment. *Ultrason. Sonochem.* **2024**, *103*, 106792.
(39) Gunalan, S.; Sivaraj, R.; Venckatesh, R. Aloe Barbadensis Miller Mediated Green Synthesis of Mono-Disperse Copper Oxide Nanoparticles: Optical Properties. *Spectrochim. Acta, Part A* **2012**, *97*, 1140−1144.

https://doi.org/10.1021/acsomega.3c10179
ACS Omega 2024, 9, 30190−30204

(40) Kumar, P. P. N. V.; Shameem, U.; Kollu, P.; Kalyani, R. L.; Pammi, S. V. N. Green Synthesis of Copper Oxide Nanoparticles Using Aloe Vera Leaf Extract and Its Antibacterial Activity Against Fish Bacterial Pathogens. *Bionanoscience* **2015**, *5* (3), 135−139.
(41) Kerour, A.; Boudjadar, S.; Bourzami, R.; Allouche, B. Eco-Friendly Synthesis of Cuprous Oxide (Cu2O) Nanoparticles and Improvement of Their Solar Photocatalytic Activities. *J. Solid State Chem.* **2018**, *263*, 79−83.
(42) Tavakoli, S.; Kharaziha, M.; Ahmadi, S. Green Synthesis and Morphology Dependent Antibacterial Activity of Copper Oxide Nanoparticles. *J. Nanostruct.* **2019**, *9* (1), 163−171.
(43) Sharma, S.; Kumar, K. Aloe-Vera Leaf Extract as a Green Agent for the Synthesis of CuO Nanoparticles Inactivating Bacterial Pathogens and Dye. *J. Dispersion Sci. Technol.* **2021**, *42* (13), 1950−1962.
(44) Eleftheriadou, I.; Giannousi, K.; Protonotariou, E.; Skoura, L.; Arsenakis, M.; Dendrinou-Samara, C.; Sivropoulou, A. Cocktail of CuO, ZnO, or CuZn Nanoparticles and Antibiotics for Combating Multidrug-Resistant Pseudomonas Aeruginosa via Efflux Pump Inhibition. *ACS Appl. Nano Mater.* **2021**, *4* (9), 9799−9810.
(45) Mansoor, S.; Shahid, S.; Javed, M.; Saad, M.; Iqbal, S.; Alsaab, H. O.; Awwad, N. S.; Ibrahium, H. A.; Zaman, S.; Sarwar, M. N.; Fatima, A. Green Synthesis of a MnO-GO-Ag Nanocomposite Using Leaf Extract of Fagonia Arabica and Its Antioxidant and Anti-Inflammatory Performance. *Nano-Struct. Nano-Objects* **2022**, *29*, 100835.
(46) Kusuma, M.; Chandrappa, G. T. Effect of Calcination Temperature on Characteristic Properties of CaMoO4 Nanoparticles. *J. Sci.: Adv. Mater. Devices* **2019**, *4* (1), 150−157.
(47) Abdelsattar, A. S.; Dawoud, A.; Helal, M. A. Interaction of Nanoparticles with Biological Macromolecules: A Review of Molecular Docking Studies. *Nanotoxicology* **2021**, *15* (1), 66−95.
(48) Waterhouse, A.; Bertoni, M.; Bienert, S.; Studer, G.; Tauriello, G.; Gumienny, R.; Heer, F. T.; de Beer, T. A.; Rempfer, C.; Bordoli, L.; Lepore, R.; Schwede, T. SWISS-MODEL: Homology Modelling of Protein Structures and Complexes. *Nucleic Acids Res.* **2018**, *46* (W1), W296−W303.
(49) Mishra, A.; Mishra, N. Antiquorum Sensing Activity of Copper Nanoparticle in Pseudomonas Aeruginosa: An In Silico Approach. *Proc. Natl. Acad. Sci. India Sect. B* **2021**, *91* (1), 29−36.
(50) Oduselu, G. O.; Ajani, O. O.; Ajamma, Y. U.; Brors, B.; Adebiyi, E. Homology Modelling and Molecular Docking Studies of Selected Substituted ((Benzo[d]Imidazol-1-Yl)Methyl)-Benzimidamide Scaffolds on Plasmodium Falciparum Adenylosuccinate Lyase Receptor. *Bioinf. Biol. Insights* **2019**, *13*, 117793221986553.
(51) Valgas, C.; Souza, S. M. d.; Smânia, E. F. A.; Smânia Jr, A. Screening Methods to Determine Antibacterial Activity of Natural Products. *Braz. J. Microbiol.* **2007**, *38* (2), 369−380.
(52) Parekh, Z. R.; Chaki, S. H.; Hirpara, A. B.; Patel, G. H.; Kannaujiya, R. M.; Khimani, A. J.; Deshpande, M. P. CuO Nanoparticles - Synthesis by Wet Precipitation Technique and Its Characterization. *Phys. B* **2021**, *610*, 412950.
(53) Halder, M.; Islam, M. M.; Ansari, Z.; Ahammed, S.; Sen, K.; Islam, S. M. Biogenic Nano-CuO-Catalyzed Facile C-N Cross-Coupling Reactions: Scope and Mechanism. *ACS Sustain. Chem. Eng.* **2017**, *5* (1), 648−657.
(54) Qamar, H.; Rehman, S.; Chauhan, D. K.; Tiwari, A. K.; Upmanyu, V. Green Synthesis, Characterization and Antimicrobial Activity of Copper Oxide Nanomaterial Derived from Momordica Charantia. *Int. J. Nanomed.* **2020**, *15*, 2541−2553.
(55) Nzilu, D. M.; Madivoli, E. S.; Makhanu, D. S.; Wanakai, S. I.; Kiprono, G. K.; Kareru, P. G. Green Synthesis of Copper Oxide Nanoparticles and Its Efficiency in Degradation of Rifampicin Antibiotic. *Sci. Rep.* **2023**, *13* (1), 14030.
(56) Ananda Murthy, H. C.; Zeleke, T. D.; Tan, K. B.; Ghotekar, S.; Alam, M. W.; Balachandran, R.; Chan, K.-Y.; Sanaulla, P. F.; Anil Kumar, M. R.; Ravikumar, C. R. Enhanced Multifunctionality of CuO Nanoparticles Synthesized Using Aqueous Leaf Extract of Vernonia Amygdalina Plant. *Results Chem.* **2021**, *3*, 100141.
(57) Cai, L.; Li, H.; Zhang, H.; Fan, W.; Wang, J.; Wang, Y.; Wang, X.; Tang, Y.; Song, Y. Enhanced Performance of the Tangerines-like CuO-Based Gas Sensor Using ZnO Nanowire Arrays. *Mater. Sci. Semicond. Process.* **2020**, *118*, 105196.
(58) Zheng, X.; Lian, Q.; Zhou, L.; Jiang, Y.; Gao, J. Peroxidase Mimicking of Binary Polyacrylonitrile-CuO Nanoflowers and the Application in Colorimetric Detection of H 2 O 2 and Ascorbic Acid. *ACS Sustain. Chem. Eng.* **2021**, *9* (20), 7030−7043.
(59) Jin, R.; Easa, J.; O'Brien, C. P. Highly Active CuO x /SiO 2 Dot Core/Rod Shell Catalysts with Enhanced Stability for the Reverse Water Gas Shift Reaction. *ACS Appl. Mater. Interfaces* **2021**, *13* (32), 38213−38220.
(60) Jabeen, S.; Siddiqui, V. U.; Rastogi, S.; Srivastava, S.; Bala, S.; Ahmad, N.; Khan, T. Fabrication of B-CuO Nanostructure and B -CuO/RGO Binary Nanocomposite: A Comparative Study in the Context of Photodegradation and Antimicrobial Activity Assessment. *Mater. Today Chem.* **2023**, *33*, 101712.
(61) Felix, S.; Chakkravarthy, R. B. P.; Grace, A. N. Microwave Assisted Synthesis of Copper Oxide and Its Application in Electrochemical Sensing. *IOP Conf. Ser. Mater. Sci. Eng.* **2015**, *73* (1), 012115.
(62) Sukumar, S.; Rudrasenan, A.; Padmanabhan Nambiar, D. Green-Synthesized Rice-Shaped Copper Oxide Nanoparticles Using Caesalpinia Bonducella Seed Extract and Their Applications. *ACS Omega* **2020**, *5* (2), 1040−1051.
(63) Tadjarodi, A.; Akhavan, O.; Bijanzad, K. Photocatalytic Activity of CuO Nanoparticles Incorporated in Mesoporous Structure Prepared from Bis(2-Aminonicotinato) Copper(II) Microflakes. *Trans. Nonferrous Metals Soc. China* **2015**, *25* (11), 3634−3642.
(64) Chand, P.; Manisha; Kumar, P. Effect of Precursors Medium on Structural, Optical and Dielectric Properties of CuO Nanostructures. *Optik* **2018**, *156*, 743−753.
(65) Iqbal, S.; Javed, M.; Bahadur, A.; Qamar, M. A.; Ahmad, M.; Shoaib, M.; Raheel, M.; Ahmad, N.; Akbar, M. B.; Li, H. Controlled Synthesis of Ag-Doped CuO Nanoparticles as a Core with Poly(Acrylic Acid) Microgel Shell for Efficient Removal of Methylene Blue under Visible Light. *J. Mater. Sci.: Mater. Electron.* **2020**, *31* (11), 8423−8435.
(66) Sharmila, G.; Sakthi Pradeep, R.; Sandiya, K.; Santhiya, S.; Muthukumaran, C.; Jeyanthi, J.; Manoj Kumar, N.; Thirumarimurugan, M. Biogenic Synthesis of CuO Nanoparticles Using Bauhinia Tomentosa Leaves Extract: Characterization and Its Antibacterial Application. *J. Mol. Struct.* **2018**, *1165*, 288−292.
(67) Singh, V.; Gupta, M. Characterisation and Zeta Potential Measurements of CuO-Water Nanofluids. In *Advances in Interdisciplinary Engineering; Select Proceedings of FLAME 2018*; Lecture Notes in Mechanical Engineering; Springer Singapore, 2019; pp 741−747.
(68) Nayeem, A.; Sitkoff, D.; Krystek, S. A Comparative Study of Available Software for High-accuracy Homology Modeling: From Sequence Alignments to Structural Models. *Protein Sci.* **2006**, *15* (4), 808−824.
(69) Khan, T.; Lawrence, A. J.; Azad, I.; Raza, S.; Khan, A. R. Molecular Docking Simulation with Special Reference to Flexible Docking Approach. *JSM Chem.* **2018**, *6* (1), 1053.
(70) Krstić, M.; Medarević, Đ.; Đuriš, J.; Ibrić, S. Self-Nanoemulsifying Drug Delivery Systems (SNEDDS) and Self-Microemulsifying Drug Delivery Systems (SMEDDS) as Lipid Nanocarriers for Improving Dissolution Rate and Bioavailability of Poorly Soluble Drugs. In *Lipid Nanocarriers for Drug Targeting*; Elsevier, 2018; pp 473−508.
(71) Raza, M.; Kanwal, Z.; Rauf, A.; Sabri, A.; Riaz, S.; Naseem, S. Size- and Shape-Dependent Antibacterial Studies of Silver Nanoparticles Synthesized by Wet Chemical Routes. *Nanomaterials* **2016**, *6* (4), 74.
(72) Stanić, V.; Tanasković, S. B. Antibacterial Activity of Metal Oxide Nanoparticles. In *Nanotoxicity*; Elsevier, 2020; pp 241−274.

https://doi.org/10.1021/acsomega.3c10179
ACS Omega 2024, 9, 30190−30204

(73) Nagaraj, E.; Karuppannan, K.; Shanmugam, P.; Venugopal, S. Exploration of Bio-Synthesized Copper Oxide Nanoparticles Using Pterolobium Hexapetalum Leaf Extract by Photocatalytic Activity and Biological Evaluations. *J. Cluster Sci.* **2019**, *30* (4), 1157−1168.
(74) Dhineshbabu, N. R.; Rajendran, V.; Nithyavathy, N.; Vetumperumal, R. Study of Structural and Optical Properties of Cupric Oxide Nanoparticles. *Appl. Nanosci.* **2016**, *6* (6), 933−939.
(75) Bansal, P.; Chaudhary, G. R.; Mehta, S. K. Comparative Study of Catalytic Activity of ZrO2 Nanoparticles for Sonocatalytic and Photocatalytic Degradation of Cationic and Anionic Dyes. *Chem. Eng. J.* **2015**, *280*, 475−485.
(76) Khan, M. A.; Nayan, N.; Shadiullah, S.; Ahmad, M. K.; Soon, C. F. Surface Study of CuO Nanopetals by Advanced Nanocharacterization Techniques with Enhanced Optical and Catalytic Properties. *Nanomaterials* **2020**, *10* (7), 1298.
(77) Jabeen, S.; Ganie, A. S.; Ahmad, N.; Hijazi, S.; Bala, S.; Bano, D.; Khan, T. Fabrication and Studies of LaFe2O3/Sb2O3 Heterojunction for Enhanced Degradation of Malachite Green Dye under Visible Light Irradiation. *Inorg. Chem. Commun.* **2023**, *152*, 110729.
(78) Hu, Y.; Chen, D.; Wang, S.; Zhang, R.; Wang, Y.; Liu, M. Activation of peroxymonosulfate by Nitrogen-Doped Porous Carbon for Efficient Degradation of Organic Pollutants in Water: Performance and Mechanism. *Sep. Purif. Technol.* **2022**, *280*, 119791.
(79) Ghasemi, S.; Rahimnejad, S.; Setayesh, S. R.; Rohani, S.; Gholami, M. R. Transition Metal Ions Effect on the Properties and Photocatalytic Activity of Nanocrystalline TiO2 Prepared in an Ionic Liquid. *J. Hazard. Mater.* **2009**, *172* (2−3), 1573−1578.
(80) Peng, Y.; Tang, H.; Yao, B.; Gao, X.; Yang, X.; Zhou, Y. Activation of Peroxymonosulfate (PMS) by Spinel Ferrite and Their Composites in Degradation of Organic Pollutants: A Review. *Chem. Eng. J.* **2021**, *414*, 128800.
(81) Saravanan, R.; Joicy, S.; Gupta, V. K.; Narayanan, V.; Stephen, A. Visible Light Induced Degradation of Methylene Blue Using CeO2/V2O5 and CeO2/CuO Catalysts. *Mater. Sci. Eng., C* **2013**, *33* (8), 4725−4731.
(82) Rana, N.; Chand, S.; Gathania, A. K. Green Synthesis of Zinc Oxide Nano-Sized Spherical Particles Using Terminalia Chebula Fruits Extract for Their Photocatalytic Applications. *Int. Nano Lett.* **2016**, *6* (2), 91−98.
(83) Sreekanth, T. V. M.; Shim, J.-J.; Lee, Y. R. Degradation of Organic Pollutants by Bio-Inspired Rectangular and Hexagonal Titanium Dioxide Nanostructures. *J. Photochem. Photobiol., B* **2017**, *169*, 90−95.
(84) Hassanpour, M.; Safardoust-Hojaghan, H.; Salavati-Niasari, M.; Yeganeh-Faal, A. Nano-Sized CuO/ZnO Hollow Spheres: Synthesis, Characterization and Photocatalytic Performance. *J. Mater. Sci.: Mater. Electron.* **2017**, *28* (19), 14678−14684.
(85) Ganesan, K.; Jothi, V. K.; Natarajan, A.; Rajaram, A.; Ravichandran, S.; Ramalingam, S. Green Synthesis of Copper Oxide Nanoparticles Decorated with Graphene Oxide for Anticancer Activity and Catalytic Applications. *Arab. J. Chem.* **2020**, *13* (8), 6802−6814.
(86) Akter, J.; Sapkota, K. P.; Hanif, M. A.; Islam, M. A.; Abbas, H. G.; Hahn, J. R. Kinetically Controlled Selective Synthesis of Cu2O and CuO Nanoparticles toward Enhanced Degradation of Methylene Blue Using Ultraviolet and Sun Light. *Mater. Sci. Semicond. Process.* **2021**, *123*, 105570.
(87) George, A.; Magimai Antoni Raj, D.; Venci, X.; Dhayal Raj, A.; Albert Irudayaraj, A.; Josephine, R. L.; John Sundaram, S.; Al-Mohaimeed, A. M.; Al Farraj, D. A.; Chen, T.-W.; Kaviyarasu, K. Photocatalytic Effect of CuO Nanoparticles Flower-like 3D Nanostructures under Visible Light Irradiation with the Degradation of Methylene Blue (MB) Dye for Environmental Application. *Environ. Res.* **2022**, *203*, 111880.
(88) Ikram, A.; Jamil, S.; Fasehullah, M. Green Synthesis of Copper Oxide Nanoparticles from Papaya/Lemon Tea Extract and Its Application in Degradation of Methyl Orange. *Mater. Innovat.* **2022**, *02* (04), 115−122.
(89) Ramesh, P.; Rajendran, A. Photocatalytic Dye Degradation Activities of Green Synthesis of Cuprous Oxide Nanoparticles from Sargassum Wightii Extract. *Chem. Phys. Impact* **2023**, *6*, 100208.
(90) Joshi, B. N.; Yoon, H.; Na, S. H.; Choi, J. Y.; Yoon, S. S. Enhanced photocatalytic performance of graphene−ZnO nanoplatelet composite thin films prepared by electrostatic spray deposition. *Ceram. Int.* **2014**, *40*, 3647−3654.

https://doi.org/10.1021/acsomega.3c10179
ACS Omega 2024, 9, 30190−30204